Error Propagation and Control in 2D and 3D Hybrid Seismic Wave Simulations for Box Tomography

Chao Lyu, Liang Zhao, Yann Capdeville, Zigen Wei

Error Propagation and Control in 2D and 3D Hybrid Seismic Wave Simulations for Box Tomography

Chao Lyu[1,2], Liang Zhao[2*], Yann Capdeville[3], Zigen Wei[4]

[1]Department of Earth and Planetary Science, University of California, Berkeley, CA, USA
[2]State Key Laboratory of Lithospheric Evolution, Institute of Geology and Geophysics, Chinese Academy of Sciences, Beijing, China
[3]Laboratoire de Planétologie et Géodynamique de Nantes, CNRS, Université de Nantes
[4]State Key Laboratory of Geodesy and Earth's Dynamics, Innovation Academy for Precision Measurement Science and Technology, Chinese Academy of Sciences, Wuhan, China

Declaration of Competing Interests: The authors acknowledge there are no conflicts of interest recorded.

Key Points:

- Standard global wave simulation yields inaccurate effective body forces, a challenge for box tomography.
- Increasing elements within the SPECFEM3D_GLOBE by 1.5 times could yield accurate hybrid simulation.
- The accurate hybrid numerical simulation lays an important forward modeling foundation for box tomography.

Corresponding author: Liang Zhao, zhaoliang@mail.iggcas.ac.cn

Abstract

To enhance the local resolution of global waveform tomography models, particularly in areas of interest within the Earth's deep structures, a higher-resolution localized tomography approach (referred to as "box tomography") is crucial for a more detailed understanding of the Earth's internal structure and geodynamics. Because the small-scale features targeted by box tomography are finer than those in global reference models, distinct spatial meshes are necessary for global and local (hybrid) forward simulations. Within the spectral element method (SEM) framework, we employ the intrinsic Lagrangian spatial interpolation to compute and store hybrid inputs (displacement/potential) in the global numerical simulation. These hybrid inputs are subsequently imposed into the localized domain during the iterative box tomography. However, inaccurate spatial Lagrange interpolation can lead to imprecise hybrid inputs, and this error can propagate from the global simulation to the hybrid simulation. It is essential to quantitatively analyze this error propagation and control it to ensure the credibility of box tomography. We introduce a unique spatial window function into the conventional "direct discrete differentiation" hybrid method. When the local mesh and structure align with those in the global simulation, the synthetic hybrid waveforms match the global ones, serving as a reference for quantitatively assessing error propagation stemming from changes in the local spatial mesh during hybrid simulation. Significantly, the relative waveform error, arising due to spatial Lagrange interpolation, is around 5% when employing the traditional SEM with five Gauss-Lobatto-Legendre (GLL) points per minimum wavelength in the 3D global simulation through SPECFEM3D_GLOBE. Ultimately, by increasing the spectral elements by about 1.5 times in the standard global simulation, we achieve hybrid waveforms with an accuracy of about 1.5%.

1 Introduction

In recent decades, owing to the development of powerful computer clusters and the extensive global deployment of receivers, global waveform tomography has obtained seismic imaging of Earth with an unprecedented resolution (French & Romanowicz, 2015; Bozdag et al., 2016; Fichtner et al., 2018; Lei et al., 2020). Numerical simulation of the elastic/acoustic wave equation for the multi-scale Earth is a key aspect of imaging techniques such as the full-waveform inversion (FWI) (Tarantola, 1984; Pratt et al., 1998; Virieux & Operto, 2009; Capdeville & Métivier, 2018; Tromp, 2019; Lyu, Capdeville, Al-Attar, & Zhao, 2021). However, capturing globally multi-scale structures by applying FWI using band-limited data (e.g., $\geq$ 1 s) requires thousands of global simulations, which are on the 4th power of frequency and computationally prohibitive.

The concept of "Box Tomography" provides a framework that holds promise for improved image solutions of target small-scale objects located in the deep Earth. In this approach, a two-step method can be adopted based on the domain decomposition as follows. A global numerical solver is used to compute the teleseismic wavefield outside of a remote target region (or "box") in the reference model with large-scale structures. The

wavefields (displacement or potential adopted in this study and named after hybrid inputs) at the box boundaries are calculated and stored as the equivalent sources and then imposed into the multi-scale local target model as the second (hybrid) simulation using a regional solver. After finishing the global simulations from the remote sources side and/or the remote receiver side once and for all, the wavefield and the models are updated only within the box at each iteration of the tomographic inversion, significantly increasing the efficiency of the imaging process (Masson & Romanowicz, 2017a, 2017b).

As the forward part of box tomography, the hybrid simulation is basic and significant. Popular hybrid simulations of wave propagation are divided into three main categories. Based on the physical representation theorem, the first category explicitly approximates surface integral(s) to obtain the physical hybrid inputs (physical quantities displacement plus traction in the elastic case), and it is referred to as the "multiple point sources method" (Monteiller et al., 2012; Tong, Chen, et al., 2014; Tong, Komatitsch, et al., 2014; Zhao et al., 2016; Wang et al., 2016; Lin et al., 2019; Meng et al., 2021). The second category constructs the numerical hybrid inputs (only displacement in the elastic case) using a spatial window function and the discrete wave equation, and it is referred to as the "direct discrete differentiation method" (Masson et al., 2014; Masson & Romanowicz, 2017b, 2017a; Clouzet et al., 2018; Adourian et al., 2022). The third category combines the physical and numerical representation theorems to calculate the combined hybrid inputs (displacement, acceleration, and traction in the elastic case), and a review of the benchmark of implementation of different hybrid methods is listed in Lyu et al. (2022). Note that only displacement/potential are needed in the second category, and they are both continuous and differentiable at the element connections under the framework of the spectral element method (SEM). It is the necessary condition we must meet when one adopts the global spatial interpolation to calculate the hybrid inputs in the global simulation, physical quantities like traction in SEM are discontinuous and non-derivable across the interfaces connected by spectral elements, and can only be calculated in the single element (Monteiller et al., 2012; Lyu et al., 2022).

Notably, in this study, we adopt the second category to perform all the hybrid simulations. For hybrid simulation with the same large-scale structures and mesh as the global simulation, it is the only hybrid method that could fully recover the local wavefield (the same as the global solution) in the sense that no additional error is introduced into the reconstructed wavefield except for the rounding errors (Masson et al., 2014). Therefore, the direct discrete differentiation method can be used as a reference method to help analyze the respective error propagation in the hybrid simulations.

In research on the forward hybrid simulation of box tomography, there are still many questions that require further exploration. The hybrid simulation is affected by the spatial- and temporal interpolation errors of both the global and hybrid simulations. However, how the accuracy of the intermediate quantity of hybrid inputs, obtained in the global Earth scale, affects the accuracy of the hybrid waveform lacks detailed analysis in the literature. The imaging resolution to be pursued in box tomography is generally finer

than that of the global reference model, so different spatial grids of the global and hybrid simulations are always needed. Under this mesh flexibility, it is still unclear whether we can obtain hybrid waveforms in the hybrid simulation the same as those in the global simulation, or whether there are errors in the hybrid inputs that are calculated and saved in the global simulation of the large-scale structure. In addition, if there is an error, the error source requires further investigation. Additional unknowns include how this error propagates from the global simulation into the hybrid simulation of multi-scale structures. As we know, the imposing operations of the hybrid inputs will be performed many times and this kind of error will be accumulated during the tomographic inversion because each hybrid simulation is independent of the other, so it is significant to reduce this error in the hybrid inputs and then perform the hybrid simulation as accurately as possible with a completely flexible local spatial mesh for the multi-scale structures. It is also significant to reduce the hardware storage of hybrid inputs obtained in the first global simulation because a large number of distant sources will be used in box tomography. All these questions are of great significance and will be discussed in this study.

The remainder of this article is structured as follows. In the methodology section, we first list the acoustic/elastic wave equations and analyze the common direct discrete differentiation hybrid method, and a slightly different hybrid method is proposed for the subsequent error analysis. Then, the associated error propagation from the global simulations of large-scale structures to the hybrid simulations of multi-scale structures is analyzed, followed by two ways to reduce this kind of error. In the subsequent numerical experiments section, a series of 2D/3D hybrid simulations of the elastic wave equation in homogeneous and heterogeneous Earth models demonstrate the validation of the proposed ways of reducing the spatial interpolation error.

2 Methodology

In this section, we present the elastic and acoustic wave equations in the Earth and a brief explanation of the principle of SEM (for a detailed introduction, please refer to Komatitsch and Vilotte (1998)). Then, the commonly used nomenclatures and the overall workflow of the hybrid simulation are described. Next, we briefly introduce the common direct discrete differentiation hybrid method "YM" (after author Yder Masson; Masson et al. (2014)), and a modified hybrid method "MYM" (the Modified YM) to be used as a reference method to subsequently analyze the source of error of hybrid simulation. The brief benchmark of these two hybrid methods and the workflow of the MYM method are listed (for their detailed benchmark, please refer to the Supplementary file).

2.1 Elastic and acoustic wave equation

In this study, we investigate the error propagation of the hybrid simulation of the elastic and acoustic wave equation. The propagation of seismic waves in the solid part

of Earth (the crust, mantle, and inner core) is governed by the equations of motion:

$$\begin{cases} \rho\ddot{\mathbf{u}} = \nabla \cdot \boldsymbol{\sigma} + \mathbf{f} \\ \boldsymbol{\sigma} = \mathbf{C} : \boldsymbol{\varepsilon} \\ \boldsymbol{\varepsilon} = \frac{1}{2}[\nabla\mathbf{u} + (\nabla\mathbf{u})^T], \end{cases} \tag{1}$$

where $\mathbf{u}(\mathbf{x}, t)$ is the displacement field vector, $\rho(\mathbf{x})$ is the density, $\boldsymbol{\sigma}(\mathbf{x})$ is the stress tensor, $\boldsymbol{\varepsilon}(\mathbf{x})$ is the strain tensor, and $\mathbf{f}(\mathbf{x}, t)$ are the body forces in the elastic domain Ω; $\mathbf{u}$ is subject to boundary conditions on $\partial\Omega$ (i.e., traction vanishes at the Earth's surface).

In the fluid part of the Earth (the ocean and outer core), the propagation of acoustic waves is supported by

$$\begin{cases} \frac{1}{\kappa}\ddot{q} = \nabla \cdot (\frac{1}{\rho}\mathbf{u}) + f \\ \mathbf{u} = \nabla q, \end{cases} \tag{2}$$

where q is the displacement potential, $\kappa(\mathbf{x})$ is the bulk modulus, $\rho(\mathbf{x})$ is the density, $\mathbf{u}(\mathbf{x}, t)$ is the displacement, $\ddot{q}$ is the second derivative of the displacement potential q with respect to time, and $f(\mathbf{x}, t)$ is a scalar source term. In general, the lossless acoustic medium is fully described by only two parameters: density $\rho(\mathbf{x})$ and speed $V(\mathbf{x})$ such that $\kappa(\mathbf{x}) = \rho(\mathbf{x})V^2(\mathbf{x})$.

2.2 Principle of SEM

SEM is a finite-element method that is based on the weak form of multiplying the wave equation with any test function. A discrete approximation of the continuous displacement $\mathbf{u}$ is required to numerically solve this weak form. Then, the original domain is discretized into nonoverlapping quadrilateral and hexahedral spectral elements in 2D and 3D cases. The numerical integration of the corresponding weak form is calculated using Gauss-Lobatto-Legendre (GLL) points (Komatitsch & Vilotte, 1998). Take the elastic wave equation as an example, the resultant matrix expression of the standard differential equation (ODE) can be written as

$$\mathbf{M}\ddot{\mathbf{U}} + \mathbf{K}\mathbf{U} = \mathbf{F}, \tag{3}$$

where $\mathbf{M}$ is the diagonal global mass matrix that can enable explicit temporal iteration and $\mathbf{K}$ is the sparse global stiffness matrix. In practical applications, $\mathbf{K}$ is not assembled but the internal force $\mathbf{KU}$ is calculated by the tensor product element by element. $\mathbf{F}$ is the source vector, and $\mathbf{U}$ and $\ddot{\mathbf{U}}$ are the unknown displacement and its acceleration vectors, respectively. Then, the Newmark scheme (Newmark, 1959) with second-order temporal accuracy is used to update $\mathbf{U}^n$, $\dot{\mathbf{U}}^n$, and $\ddot{\mathbf{U}}^n$ to $\mathbf{U}^{n+1}$, $\dot{\mathbf{U}}^{n+1}$, and $\ddot{\mathbf{U}}^{n+1}$, respectively, as follows:

$$\begin{cases} \mathbf{U}^{n+1} = \mathbf{U}^n + \Delta t\dot{\mathbf{U}}^n + 0.5\Delta t^2\ddot{\mathbf{U}}^n \\ \dot{\mathbf{U}}^{n+1} = \dot{\mathbf{U}}^n + 0.5\Delta t\left[\ddot{\mathbf{U}}^n + \ddot{\mathbf{U}}^{n+1}\right] \\ \ddot{\mathbf{U}}^{n+1} = \mathbf{M}^{-1}(\mathbf{F}^{n+1} - \mathbf{K}\mathbf{U}^{n+1}). \end{cases} \tag{4}$$

2.3 Nomenclatures and workflow for the hybrid simulation

The nomenclatures often used in the hybrid simulation are illustrated below and displayed in Figure 1. These mainly include the domains (Ω_g, Ω_e, and Ω_l), models (M_{g0}, M_{g1}, M_{e0}, M_{l0}, and M_{l1}), and the hybrid interface S.

1. ***Domains***: Ω_g represents the ***Global Domain*** containing the ***Local Domain*** (closed box inside the global domain) Ω_l, and the ***External Domain*** Ω_e. It should be noted that $\Omega_e + \Omega_l = \Omega_g$ for the domains.
2. ***Models***: M_{g0} represents the known 1D or 3D ***Global Reference Model*** with large-scale structures from previous studies assigned to the global domain Ω_g and includes the known ***External Model*** M_{e0} and ***Local Reference Model*** M_{l0}. M_{g1} is the ***Global Target Model*** also assigned to the global domain Ω_g, and includes the known external model M_{e0} and the unknown ***Local Target Model*** M_{l1} with small-scale structures. It is important to note that $M_{e0} + M_{l0} = M_{g0}$ and $M_{e0} + M_{l1} = M_{g1}$ for the models.
3. ***Hybrid Interface*** S: the interface separates the external domain Ω_e and the local domain Ω_l.

It is worth noting that the external model M_e is assumed to be unperturbed during iterative box tomography. The workflow for forward solving the wave equation in box tomography is based on the hybrid simulation. For the case with a source outside and a receiver inside or outside the local domain, the hybrid simulation involves the following two or three steps of modeling:

1. First, we calculate and save the hybrid inputs using a global solver in the global reference model M_{g0} from the source side.
2. Then, we impose the hybrid inputs recorded in the first step into the local target model M_{l1} as the equivalent sources and perform a hybrid simulation of multi-scale structures using a local numerical solver. At the same time, we obtain the hybrid outputs due to the existence of local anomalies.
3. In the final, if the receiver is positioned outside the localized box, we calculate and save the Green's Functions using a global solver in a global reference model M_{g0} from the remote receiver side. After that, we can get the residual hybrid waveform by the convolution between hybrid outputs and Green's Functions.

One of the targets of our study is to determine how the error of hybrid inputs is propagated from the global simulation to the hybrid simulations. To help analyze the error propagation in detail, we need a hybrid method that does not generate any error (except for rounding error) during the hybrid simulation when the global and local structure and mesh are the same. The following subsection briefly elaborates on the two slightly different direct discrete differentiation methods.

2.4 Hybrid methods

In the 2D/3D heterogeneous background models, Bielak et al. (2003) and Yoshimura et al. (2003) directly operate on the discrete wave equation using an auxiliary variable (scattered wavefield) and obtain hybrid inputs in the temporally implicit finite element method framework. Masson et al. (2014) utilize this method of calculating the hybrid inputs and propose a more compact numerical hybrid method in a temporally explicit SEM framework using a window function. Hereafter, we refer to this method as the "YM" hybrid method. The conceptual illustration of the local target model M_{l1} associated with the YM method is displayed in Figure 1b. The explicit mathematic expression of the hybrid inputs $\mathbf{F}^l$ can be derived as:

$$\begin{aligned} \mathbf{F}^l &= \mathbf{W}\cdot\mathbf{F} - \mathbf{W}\cdot(\mathbf{K}\cdot\mathbf{U}) + \mathbf{K}\cdot(\mathbf{W}\cdot\mathbf{U}) \\ &= \sum_e \Big(\mathbf{W}^e\cdot\mathbf{F}^e - \mathbf{W}^e\cdot(\mathbf{K}^e\cdot\mathbf{U}^e) + \mathbf{K}^e\cdot(\mathbf{W}_e\cdot\mathbf{U}^e) \Big), \end{aligned} \tag{5}$$

where $\sum_e$ denotes the assembly of all the elemental with nonzero hybrid inputs using the SEM, $\mathbf{U}^e$, $\mathbf{K}^e$, $\mathbf{U}$, and $\mathbf{K}$ are the elemental and assembled potential/displacement vectors and stiffness matrices, respectively, and $\mathbf{W}^e$ and $\mathbf{W}$ are the elemental and assembled diagonal matrix that acts as the discrete window function used to choose the *GLL* points for the hybrid simulation. In this study, we propose a modified YM (MYM) hybrid method in Figure 1c by using a different window function. The new window function is defined and plotted in the Supplementary file. Please consult the Supplementary file for a detailed benchmark comparison between the YM and MYM hybrid methods.

2.5 Error propagation and control

Based on the proposed MYM hybrid method, we further investigate how the error is propagated from the global simulation to the hybrid simulation, under the framework of the 2D acoustic wave equation. The full regeneration of the hybrid wavefield depicted in Figure 2abd and the hybrid waveforms presented in Figure 3a show that the MYM hybrid method does not introduce any error except for the rounding error during the imposing of hybrid inputs when the local and global mesh and structures are the same. However, when the local and global structures are the same and their mesh is different, the hybrid inputs obtained by the MYM hybrid method will carry inevitable errors, leading to the regeneration with errors of the hybrid wavefield and waveform, as shown in Figure 2ce and Figure 3b. The only difference between these two cases is the usage of the different *GLL* points from the different hybrid elements of the same local model to calculate the hybrid inputs with the spatial Lagrange wavefield interpolation.

To analyze and determine ways to reduce this error, we first evaluate the analytical precision of Lagrange wavefield interpolation of different global mesh. We aim to determine why and how the inaccurate Lagrange wavefield interpolation affects the precision of the hybrid inputs. The error analysis in Figure 4 shows that the Lagrange wavefield interpolation upsampling wavefields from coarse spectral elements to fine spectral elements is not appropriately accurate, thereby introducing errors into the hybrid inputs

(the potential or displacement calculated by Lagrange interpolation) and thus leading to inaccurate hybrid waveform in the hybrid simulation. In Figure 4, the reverse solid black triangles represent the values of the $\cos(\pi x)$ function at the GLL points in the reference element $[-1,\ 1]$. The red points represent the output points between $[-1,\ 1]$ by the spatial Lagrange interpolation of the solid black triangles. The residual error enlarged by a factor of times between the interpolated values in red points and the accurate $\cos(\pi x)$ values in black circles is shown as blue points. Figure 4a illustrates that the relative interpolation error with a traditional SEM with $NGLL = 5$ in each element could be as large as 3.89%, e.g., when calculating the waveform of a given receiver in an element, or calculating the hybrid inputs of all the local GLL points during the global simulation. The relative interpolation error is calculated by the ratio between the L1 norm of the residual waveform (difference between the interpolated and accurate $cos(x)$ function) and the L1 norm of the accurate $cos(x)$ function.

Figures 4b and 4c illustrate the two proposed methods for decreasing the Lagrange interpolation error using more spectral elements (e.g., two elements per minimum wavelength, $G = 9$ with $NGLL = 5$ in Figure 4b) or a high-order spectral element to perform the global simulation and Lagrange interpolation (e.g., $G = 8$ with $NGLL = 8$ in Figure 4c). The corresponding relative errors are 0.62% and 0.18%, respectively, which are acceptable and much smaller than the traditional case shown in Figure 4a ($G = 5$ with $NGLL = 5$). For the second method, to offer more references, we also find that interpolated errors by Lagrange interpolation with $NGLL = 5$, 6, 7, 8, 9, and 10 in one element per minimum wavelength are approximately 3.89%, 3.92%, 0.17%, 0.18%, 0.0049%, and 0.0052%, respectively. Although the interpolated accuracy of an even order (say $N = 4$) is almost the same as that of an odd order (say $N = 5$), the relative error of the simulated hybrid waveform is larger because fewer numerical integration GLL points are used to compute the mass and stiffness matrices.

In the supplementary file, we adopt a series of hybrid simulations to quantify how the error propagates from the global simulation to the hybrid simulation and how the error can be controlled in the proposed two ways, under the framework of 2D acoustic hybrid simulation. However, in global seismology, increasing the polynomial degree significantly extremely reduces the available time step for numerical simulations, due to the thickness of the Earth's Crust generally being much smaller than the minimum wavelength. Note that the available time step is inversely proportional to the square of the spectral element polynomial order (Lyu et al., 2020). Thus the first method by increasing the number of elements will be more suitable in the global simulation for calculating the hybrid inputs. In the future, when we can easily conduct very high-frequency (≈ 1 Hz) global and hybrid numerical simulations of the Earth models, increasing the polynomial degree within the elements will also be a very efficient method.

3 Numerical experiments

To numerically validate the proposed MYM hybrid method and apply the proposed way to control the error of hybrid simulation, we conduct a series of 2D and 3D hybrid numerical simulations with the PREM (Dziewonski & Anderson, 1981) as the background model.

3.1 2D hybrid simulations in the PREM model

First, we validate the method's applicability in a 2D Earth model under two scenarios: one with the source outside and the receiver inside the box (referred to as SORI), and the other with both the source and receiver located outside the box (referred to as SORO). Then, we assess the different accuracies of hybrid simulations using various maximum frequency sources, while with invariable settings of the global and local model and mesh.

In this 2D case, we select part of PREM as our global and local reference models. The global mesh is different from the local mesh in the local domain. The global and local simulation involves a free surface, and 10 elements are used for the absorbing boundary condition near the left, right, and bottom boundaries, as illustrated in Figure 5. To verify the proposed algorithm, we construct a localized Gaussian anomaly below the surface, as detailed in Figure 5c. As in simulating a real application scenario, a constant stable Courant number 0.5 is used both in all the global and local simulations. The time step of all the following global simulations of each Ricker wavelet with different frequency bands is the same 0.081 s, and the time step of all the local simulations is 0.047 s because the mesh of the local model is denser than the global one. So the waveform difference due to the different time steps of the global and local time steps will be the same for all sets of global and local simulations with different minimum periods. The global mesh is designed based on a minimum period of 6 seconds ($NGLL$=6, points per wavelength G=6). The ocean part of the PREM model (Dziewonski & Anderson, 1981) is replaced with the crust below.

Figure 6 presents the global and hybrid wavefields at around 1100 seconds. Even though the mesh is designed with a parameter of $G = 6$ for the S wave, some spatial dispersion error is noticeable after the surface wave in Figure 6a. Notably, in Figure 6b, scattered waves are seen extending beyond the boundary, primarily due to inaccuracies in the hybrid inputs for the S wave with a similar wavelength to the element, as indicated by the black arrows. Apart from the previously marked scattered waves on both sides in Figure 6c, there is a noticeable outgoing phase at the bottom due to a local Gaussian anomaly, marked by the black arrow. These scattered waves are employed for calculating the waveforms at receivers outside the boundary through convolution (Adourian et al., 2022). To perform the hybrid simulation accurately for the S-wave phases, we need to increase the number of elements in the global model, as proposed in the above section, to provide more accurate hybrid inputs. Thus, the number of elements required for

a global simulation in the box tomography would exceed the number utilized in a standard numerical simulation.

Figures 7 and 8 are the waveforms and associated errors of the receivers inside and outside the local model in various frequency bands under the background PREM. From the bottom to the upper, the minimum periods of the ricker wavelet are from 6 s to 11.6 s. For the PREM model, we first conduct a spatial global mesh for calculating the minimum period of about 6 seconds. Once the model's mesh is fixed, as we gradually increase the minimum period of the simulation, it becomes evident that errors decrease. The hybrid waveforms in Figure 8 are computed by adding the waveform obtained from the global reference model to the scattered waveform. The scattered waveform of the receiver outside the local domain is obtained by the convolution between the scattered hybrid outputs forces and Green's Functions of the GLL points, which are shown in red in Figure 8abc. For details on the convolution calculation of the hybrid waveform resulting from the local anomaly between a remote source and a remote receiver, please refer to Adourian et al. (2022). This example demonstrates the significant importance of increasing the number of elements in global simulations for practical 2D applications of hybrid simulations. In the SORI case, the error is decreased from about 10% to 1.5% for the x component. In the SORO case, the error is decreased from about 3.25% to 0.5% for the x component. Hybrid waveforms with around 1.5% accuracy can be obtained with the hybrid inputs from the global simulation in the program SPECMAT (Spectral Element Method in Matlab, used in Lyu et al. (2022)) by increasing the number of spectral elements required for standard numerical simulation by about 1.5 times (from 6 s to about 9 s), as shown in Figures 7 and 8. Note that the remaining errors, such as the Ux error below 1.5% in SORI, should be explainable by the different temporal dispersion errors of global and local simulations because the spatial-dispersion error and temporal-dispersion error are independent of each other (Lyu, Capdeville, Lu, & Zhao, 2021). It demonstrates the significant importance of increasing the number of elements in global simulations under the framework of hybrid simulation in box tomography, both for receivers located inside and outside the box.

3.2 3D hybrid simulations in the PREM model

In this section, we further validate the way of controlling the error of hybrid simulation in the PREM model with 3D hybrid simulation under the SORI case. We use different local and global mesh configurations, following the same procedure as in the above subsection.

The program SPECFEM3D_GLOBE is used to calculate hybrid inputs within the PREM Earth model, with the ocean part replaced by the upper crust. Note that the global mesh in SPECFEM3D_GLOBE is unstructured, unlike the local mesh within the confined domain. So spatial interpolation is required to calculate the hybrid inputs for hybrid simulation. A remote source is located at $(40°, 0°, 6271km)$, 100 km below the Earth's surface, defined by latitude, longitude, and the Cartesian height coordinate. Inside the

local domain, we place a single receiver on the Earth's surface. A filtered Heaviside wavelet source with four cutoff corner periods is used. Each global and hybrid simulation pair uses a different source but retains the global and local mesh configurations. Specifically, the first cutoff corner period ranges from 27, 30 to 48 s, while the other three remain fixed at 53, 250, and 400 s.

In the hybrid simulations, we consider a free surface, and four elements are used to apply absorbing boundary conditions near the five boundaries: left, right, front, back, and bottom, as illustrated in Figure 9a. To validate our proposed way of controlling the error propagation from the 3D global numerical simulation to the hybrid numerical simulation, we use a consistent global time step of 0.1425 s for all global simulations and a local time step of 0.2 s for all hybrid simulations. Similar to the 2D case, this ensures that the temporal dispersion error differences between the global and corresponding hybrid simulations pair are consistent. The global mesh is designed based on the number of spectral elements along one side of a chunk in the cubed sphere (NEX_XI=160), which is accurate to the shortest period of roughly 27 seconds. The hybrid GLL points displayed in black in Figure 9a, are used to impose the hybrid inputs, which are obtained by the program SPECFEM3D_GLOBE from the teleseismic event. Figure 9bcd displays the hybrid wavefields corresponding to arrival times of P, S, and Surface wave phases respectively. Figure 10 illustrates the waveforms of three components and associated errors of the receivers inside the local model in various frequency bands in the PREM model. From the bottom to the upper, the first cutoff corner periods of the Heaviside wavelet are from 27, 30 to 48 s. The error decreases from about 5% to 1.5%. Hybrid waveforms with around 1.5% accuracy can be obtained with hybrid inputs obtained from the global simulation in the program SPECFEM3D_GLOBE by increasing the number of spectral elements required for standard numerical simulation by 1.5 times (from 27 s to about 40 s). The remaining $\approx 1.5\%$ of the SORI waveforms can be explained by the different temporal dispersion errors in global and local simulations. It demonstrates the significant importance of increasing the number of elements in global simulations in the program SPECFEM3D_GLOBE for practical 3D applications of hybrid simulations during box tomography.

4 Discussion

4.1 Credibility of Box Tomography

Box Tomography is specifically designed to enhance the resolution of targeted localized domains that exhibit richer or better data illustration compared to those used in global waveform tomography. Additionally, Global waveform tomography is obtained by the global minima of the misfit between the synthetics and real data. However, Box Tomography focuses on the minima solely within the localized box domain. The medium outside the box is the 3D reference model from global waveform tomography (e.g. GLAD_M25, SEMUCB_WM1), they are not ideally spherically symmetric (with the ellipticity, topography, and ocean mass load). The 3-D reference models are generated using band-limited real waveform data at approximately 20 seconds. The globally distributed small-scale

structures have been proven to contribute effectively to smooth anisotropic structures (Capdeville & Métivier, 2018). Ensuring the credibility of box tomography requires alignment between the structures defining the boundaries of the box and those of the global 3D tomography. Multi-scale structures, such as the subducting slabs, have been effectively replaced by smooth structures, maintaining consistency between the global model and the box boundaries. In addressing the solid-fluid coupling at the ocean-continent boundary, core-mantle boundary, and inner-core boundary, incorporating identical solid and fluid structures at the box's boundary same as the global model is an important step to be solved under the framework of box tomography.

4.2 Error propagation and control

Through the proposed MYM hybrid method and the error analysis of the hybrid simulations, we can now answer all the questions raised in the Introduction section. When the local and global models have the same structures and meshes, we can obtain the same hybrid waveform in the hybrid simulation as the global simulation. However, when the mesh is different between the local and global models, even for the same structures, the hybrid inputs that are calculated and saved in the global simulation still have errors. The source of this error originates from the inaccurate spatial Lagrange interpolation of the potentials of the GLL points. The obtained hybrid inputs with error, as the equivalent sources, are imposed into the hybrid simulation of the multi-scale structures, leading to hybrid waveforms with error. To reduce the error of the hybrid inputs and then perform the hybrid simulation as accurately as possible with a completely flexible spatial mesh in the local multi-scale structures, we suggest two methods: i) increase the number of elements with traditional $NGLL = 5$ in the global simulation, and ii) increase the polynomial degree of the global mesh. However, for the second method, there are limitations in the case of global seismology because considering very thin crust results in extremely small time steps.

4.3 Computational cost

For the computational complexity analysis of the hybrid simulation, if the local target structures are large-scale, the computational complexity of our proposed hybrid simulation is proportional to λ_{min}^4 (minimum wavelength), including three spatial dimensions and one temporal dimension. In this kind of hybrid simulation with the same local mesh as that in the global simulation, only the displacements and internal forces of the GLL points exactly on the hybrid interface are needed. Thus, this is memory-saving and suitable for 3D hybrid simulation owing to the 2D distribution of the related hybrid inputs.

If the local target structures are small-scale, which is much smaller than λ_{min}, for instance, being one-tenth the size of the background large-scale structures. A lower-degree SEM (such as $N = 1$ or 2) can be used to precisely describe the model, ensure the accuracy of the simulation, and simultaneously reduce the computational complexity. Ow-

ing to the locally limited domain, we can limit the costly simulation to a small region, avoiding computation over the entire space. To save the corresponding memory storage of the hybrid inputs in the first global simulation, the hybrid inputs of all the GLL points in the hybrid elements are required. The memory of the hybrid inputs is acceptable if a lower-degree SEM (such as $N = 2$) is used because it will be proportional to N^3 for the 3D hybrid simulations.

4.4 Temporal compression

In this study, we do not discuss the impact of time-domain compression storage of numerical hybrid inputs on the hybrid simulations. In an ideal scenario, the time step employed in the local simulation remains entirely independent of the global time step. Within the local simulation, hybrid inputs undergo interpolation or recovery to align with a locally optimal time step for a specific target structure. However, note that when dealing with high upsampling ratios, the conventional spline interpolation method (Monteiller et al., 2020), as demonstrated by Zhang and Yao (2017), faces limitations. To address this challenge, Shen et al. (2022) introduced Fourier interpolation into the framework of hybrid simulation within the time domain, incorporating tapering operations at the end of each time series. Their work exhibits promising results in terms of achieving compressed ratios. Based on previous research (Adourian et al., 2022), we can achieve compression storage at twice the Nyquist sampling rate using B-spline interpolation. Then, during hybrid numerical simulations, we can resample the compressed hybrid inputs according to the distribution of the local meshing. Existing hybrid numerical simulations have shown that this compression storage and recovery almost do not introduce additional errors to hybrid inputs, leading to very accurate hybrid waveforms (Adourian et al., 2022). Furthermore, the time compression algorithm can be naturally combined with the way of reducing the spatial-dispersion error by increasing the number of elements or polynomial degrees in the global simulation during the proposed hybrid numerical simulation method.

4.5 Absorbing condition

Regarding local models containing anomalies, we need to implement the absorbing boundary or layer conditions to absorb the scatter waves going outside. However, the development of stable and highly efficient perfectly matched layers (PML, (Xie et al., 2014)) with good adaptability for models with complex geometry remains an open question. For rectangle PML meshes, as we use in the 2D acoustic cases in the supplementary file, the PML absorption works very well and is stable. However, for 2D/3D Earth models, we use absorption layer boundary conditions (Kosloff & Kosloff, 1986) because they are more stable than PML but require more elements for absorption compared to PML. To better fit the real data shortly, our solver SPECMAT for hybrid numerical simulation needs to implement the same attenuation expression as the program SPECFEM3D_GLOBE.

4.6 Second-order scattering

The MYM hybrid method proposed in this study only works on a 1st-order problem, not on a 2nd-order problem. Because the outgoing scattered waveform will be absorbed by the absorbing layers, and can't propagate outside of the domain and scatter with the outside heterogeneities. However, considering the geometry and material attenuation of wave propagation, and the relatively long period data used, the amplitude of the second-order scattering, compared to the 1st-order scattering, could be safely neglected. Note that for studies involving extremely high frequencies (e.g., 2Hz), further research and discussion are needed on the second-order scattering in hybrid numerical simulations, owing to the inaccurate 1D/3D background models. Nevertheless, second-order scattering often exhibits a delayed arrival compared to first-order scattering, and researchers typically focus on studying first-order scattering.

4.7 Generality

It should be noted that this study focuses only on the hybrid simulation and error propagation of seismic cases using the SEM. However, the proposed ways of increasing the number of elements or polynomial degrees, and fixing the global and local meshes but changing the minimum period, are universal and can be used to understand the error propagation of other numerical methods, such as the finite difference method (Pienkowska et al., 2020). The proposed MYM hybrid method and ways of controlling the error of hybrid simulations can also be directly used to implement the accurate hybrid simulation of the visco-elastic wave equation or more widely used to study Maxwell's equation.

5 Conclusion

By analyzing the conventional direct discrete differentiation hybrid method (YM method), we propose a slightly modified version (MYM method) by introducing a new spatial window function and combining it with the spatial Lagrange wavefield interpolation, which is well-designed for hybrid simulations in local multi-scale structures. Compared with the global brute-force calculation, the computational complexity of these methods is substantially reduced owing to the large reduction of the computational domain. The different simulated results of the proposed hybrid method indicate that the imperfect Lagrange interpolation results in inaccurate hybrid inputs and introduces certain but controllable errors propagated in the hybrid simulations. In global seismology, this error can be reduced by increasing the number of elements of standard simulation by 1.5 times, and accurate waveforms for the stations inside and outside the box can be achieved, laying an important foundation for box tomography with real data.

6 Data and Resources

All data used in this paper came from published sources listed in the references. In the Electronic Supplementary Material, we initially enumerate the intricate distinc-

tions between the preceding YM and the newly proposed MYM hybrid methods. Subsequently, we delve into the analysis of relative hybrid waveform errors through a sequence of global and hybrid simulations. Finally, to furnish a benchmark for the hybrid numerical simulation of three-dimensional elastic wave propagation, we present hybrid numerical simulations featuring both large-scale and small-scale anomalies within a two-dimensional homogeneous acoustic background model.

Acknowledgments

The authors would like to sincerely thank Professor Barbara Romanowicz from the University of California, Berkeley, and Professors Jinhai Zhang, Lei Zhang, and Youshan Liu from the Institute of Geology and Geophysics, Chinese Academy of Sciences for their fruitful discussions on the hybrid simulation and box tomography. This study is supported by the National Natural Science Foundation of China (Grant No. 41888101), the B-type Strategic Priority Program of the Chinese Academy of Sciences (Grant No. XDB41000000 and XDB42020102), the National Science Foundation (EAR-1758198), the Young Scientists Fund of the National Natural Science Foundation of China (Grant No. 42004045) and the China Scholarship Council (File No. 201804910289).

References

Adourian, S., Lyu, C., Masson, Y., Munch, F., & Romanowicz, B. (2022, 10). Combining different 3-D global and regional seismic wave propagation solvers towards box tomography in the deep Earth. *Geophysical Journal International*, *232*(2), 1340-1356. Retrieved from https://doi.org/10.1093/gji/ggac394 doi: 10.1093/gji/ggac394

Bielak, J., Loukakis, K., Hisada, Y., & Yoshimura, C. (2003). Domain reduction method for three-dimensional earthquake modeling in localized regions, part i: Theory. *Bulletin of the Seismological Society of America*, *93*(2), 817-824.

Bozdag, E., Peter, D., Lefebvre, M., Komatitsch, D., Tromp, J., Hill, J., ... Pugmire, D. (2016). Global adjoint tomography: first-generation model. *Geophysical Journal International*, *207*. Retrieved from https://doi.org/10.1093/gji/ggw356 doi: 10.1093/gji/ggw356

Capdeville, Y., & Métivier, L. (2018). Elastic full waveform inversion based on the homogenization method: theoretical framework and 2-d numerical illustrations. *Geophysical Journal International*, *213*(2), 1093-1112. Retrieved from http://dx.doi.org/10.1093/gji/ggy039 doi: 10.1093/gji/ggy039

Clouzet, P., Masson, Y., & Romanowicz, B. (2018, 02). Box Tomography: first application to the imaging of upper-mantle shear velocity and radial anisotropy structure beneath the North American continent. *Geophysical Journal International*, *213*(3), 1849-1875. Retrieved from https://doi.org/10.1093/gji/ggy078 doi: 10.1093/gji/ggy078

Dziewonski, A. M., & Anderson, D. L. (1981). Preliminary reference earth model. *Physics of the earth and planetary interiors*, *25*(4), 297–356.

Fichtner, A., van Herwaarden, D.-P., Afanasiev, M., Simutė, S., Krischer, L., Çubuk Sabuncu, Y., ... Igel, H. (2018). The collaborative seismic earth model: Generation 1. *Geophysical Research Letters*, *45*(9), 4007-4016. Retrieved from https://agupubs.onlinelibrary.wiley.com/doi/abs/10.1029/2018GL077338 doi: 10.1029/2018gl077338

French, S. W., & Romanowicz, B. (2015). Broad plumes rooted at the base of the earth's mantle beneath major hotspots. *Nature*, *525*(7567), 95-99. Retrieved from https://doi.org/10.1038/nature14876 doi: 10.1038/nature14876

Komatitsch, D., & Vilotte, J.-P. (1998). The spectral element method : an effective tool to silmulate the seismic response of 2d and 3d geological structures. *Bulletin of the seismologic Society of America*, *88*(2), 368-392.

Kosloff, R., & Kosloff, D. (1986). Absorbing boundaries for wave propagation problems. *Journal of Computational Physics*, *63*(2), 363-376. Retrieved from https://www.sciencedirect.com/science/article/pii/0021999186901993 doi: https://doi.org/10.1016/0021-9991(86)90199-3

Lei, W., Ruan, Y., Bozdağ, E., Peter, D., Lefebvre, M., Komatitsch, D., ... Pugmire, D. (2020). Global adjoint tomography–model GLAD-M25. *Geophysical Journal International*, *223*(1), 1-21. Retrieved from https://doi.org/10.1093/gji/ggaa253 doi: 10.1093/gji/ggaa253

Lin, C., Monteiller, V., Wang, K., Liu, T., Tong, P., & Liu, Q. (2019). High-frequency seismic wave modelling of the deep earth based on hybrid methods and spectral-element simulations: a conceptual study. *Geophysical Journal International*, *219*(3), 1948-1969. Retrieved from https://doi.org/10.1093/gji/ggz413 doi: 10.1093/gji/ggz413

Lyu, C., Capdeville, Y., Al-Attar, D., & Zhao, L. (2021, 04). Intrinsic non-uniqueness of the acoustic full waveform inverse problem. *Geophysical Journal International*, *226*(2), 795-802. Retrieved from https://doi.org/10.1093/gji/ggab134 doi: 10.1093/gji/ggab134

Lyu, C., Capdeville, Y., Lu, G., & Zhao, L. (2021). Removing the Courant-Friedrichs-Lewy stability criterion of the explicit time-domain very high degree spectral-element method with eigenvalue perturbation. *Geophysics*, *86*(5), T411-T419. Retrieved from https://doi.org/10.1190/geo2020-0623.1 doi: 10.1190/geo2020-0623.1

Lyu, C., Capdeville, Y., & Zhao, L. (2020). Efficiency of the spectral element method with very high polynomial degree to solve the elastic wave equation. *Geophysics*, *85*(1), T33-T43. Retrieved from https://doi.org/10.1190/geo2019-0087.1 doi: 10.1190/geo2019-0087.1

Lyu, C., Zhao, L., & Capdeville, Y. (2022). Novel hybrid numerical simulation of the wave equation by combining physical and numerical representation theorems and a review of hybrid methodologies. *Journal of Geophysical Research: Solid Earth*, *127*(5), e2021JB022368. Retrieved from https://agupubs.onlinelibrary.wiley.com/doi/abs/10.1029/2021JB022368 doi: https://doi.org/10.1029/2021JB022368

Masson, Y., Cupillard, P., Capdeville, Y., & Romanowicz, B. (2014). On the numerical implementation of time-reversal mirrors for tomographic imaging. *Geophysical Journal International*, *196*(3), 1580-1599. Retrieved from https://hal.archives-ouvertes.fr/hal-01303023 doi: 10.1093/gji/ggt459

Masson, Y., & Romanowicz, B. (2017a). Box tomography: localized imaging of remote targets buried in an unknown medium, a step forward for understanding key structures in the deep earth. *Geophysical Journal International*, *211*(1), 141-163. Retrieved from https://dx.doi.org/10.1093/gji/ggx141 doi: 10.1093/gji/ggx141

Masson, Y., & Romanowicz, B. (2017b). Fast computation of synthetic seismograms within a medium containing remote localized perturbations: a numerical solution to the scattering problem. *Geophysical Journal International*, *208*(2), 674-692. Retrieved from http://dx.doi.org/10.1093/gji/ggw412 doi: 10.1093/gji/ggw412

Meng, W., Yang, D., Dong, X., & Ma, J. (2021, 08). A 3D Optimized Frequency–Wavenumber (FK), Time–Space Optimized Symplectic (TSOS) Hybrid Method for Teleseismic Wave Modeling. *Bulletin of the Seismological Society of America*, *111*(6), 3403-3419. Retrieved from https://doi.org/10.1785/0120210040 doi: 10.1785/0120210040

Monteiller, V., Beller, S., Plazolles, B., & Chevrot, S. (2020, 12). On the validity of the planar wave approximation to compute synthetic seismograms of teleseismic body waves in a 3-D regional model. *Geophysical Journal International*, *224*(3), 2060-2076. Retrieved from https://doi.org/10.1093/gji/ggaa570 doi: 10.1093/gji/ggaa570

Monteiller, V., Chevrot, S., Komatitsch, D., & Fuji, N. (2012, 11). A hybrid method to compute short-period synthetic seismograms of teleseismic body waves in a 3-D regional model. *Geophysical Journal International*, *192*(1), 230-247. Retrieved from https://doi.org/10.1093/gji/ggs006 doi: 10.1093/gji/ggs006

Newmark, N. M. (1959). A method of computation for structural dynamics..

Pienkowska, M., Monteiller, V., & Nissen-Meyer, T. (2020, 11). High-frequency global wavefields for local 3-D structures by wavefield injection and extrapolation. *Geophysical Journal International*, *225*(3), 1782-1798. Retrieved from https://doi.org/10.1093/gji/ggaa563 doi: 10.1093/gji/ggaa563

Pratt, R. G., Shin, C., & Hick, G. (1998). Gauss–newton and full newton methods in frequency–space seismic waveform inversion. *Geophysical Journal International*, *133*(2), 341-362.

Shen, H., Tang, X., Lyu, C., & Zhao, L. (2022). Spatial- and temporal-interpolations for efficient hybrid wave numerical simulations. *Frontiers in Earth Science*, *10*. Retrieved from https://www.frontiersin.org/articles/10.3389/feart.2022.977063 doi: 10.3389/feart.2022.977063

Tarantola, A. (1984). Inversion of seismic reflection data in the acoustic approximation. *Geophysics*, *49*(8), 1259-1266. Retrieved from https://doi.org/10

.1190/1.1441754 doi: 10.1190/1.1441754

Tong, P., Chen, C.-w., Komatitsch, D., Basini, P., & Liu, Q. (2014). High-resolution seismic array imaging based on an sem-fk hybrid method. *Geophysical Journal International*, *197*(1), 369-395. Retrieved from http://dx.doi.org/10.1093/gji/ggt508 doi: 10.1093/gji/ggt508

Tong, P., Komatitsch, D., Tseng, T., Hung, S., Chen, C., Basini, P., & Liu, Q. (2014). A 3-d spectral-element and frequency-wave number hybrid method for high-resolution seismic array imaging. *Geophysical Research Letters*, *41*(20), 7025-7034.

Tromp, J. (2019). Seismic wavefield imaging of earth's interior across scales. *Nature Reviews Earth & Environment*. Retrieved from https://doi.org/10.1038/s43017-019-0003-8 doi: 10.1038/s43017-019-0003-8

Virieux, J., & Operto, S. (2009). An overview of full-waveform inversion in exploration geophysics. *Geophysics*, *74*(6), WCC1-WCC26. Retrieved from https://doi.org/10.1190/1.3238367 doi: 10.1190/1.3238367

Wang, Y., Chevrot, S., Monteiller, V., Komatitsch, D., Mouthereau, F., Manatschal, G., ... Martin, R. (2016). The deep roots of the western pyrenees revealed by full waveform inversion of teleseismic p waves. *Geology*, *44*(6), 475. Retrieved from +http://dx.doi.org/10.1130/G37812.1 doi: 10.1130/G37812.1

Xie, Z., Komatitsch, D., Martin, R., & Matzen, R. (2014). Improved forward wave propagation and adjoint-based sensitivity kernel calculations using a numerically stable finite-element pml. *Geophysical Journal International*, *198*(3), 1714-1747. Retrieved from https://doi.org/10.1093/gji/ggu219 doi: 10.1093/gji/ggu219

Yoshimura, C., Bielak, J., Hisada, Y., & Fernández, A. (2003, 04). Domain Reduction Method for Three-Dimensional Earthquake Modeling in Localized Regions, Part II: Verification and Applications. *Bulletin of the Seismological Society of America*, *93*(2), 825-841. Retrieved from https://doi.org/10.1785/0120010252 doi: 10.1785/0120010252

Zhang, J., & Yao, Z. (2017). Exact local refinement using fourier interpolation for nonuniform-grid modeling. *Earth and Planetary Physics*, *1*(1), 58-62. Retrieved from https://www.eppcgs.org/en/article/doi/10.26464/epp2017008 doi: 10.26464/epp2017008

Zhao, M., Capdeville, Y., & Zhang, H. (2016). Direct numerical modeling of time-reversal acoustic subwavelength focusing. *Wave Motion*, *67*, 102-115. Retrieved from http://www.sciencedirect.com/science/article/pii/S0165212516300877 doi: https://doi.org/10.1016/j.wavemoti.2016.07.010

7 Full mailing address for each author

1. Chao Lyu
Email: lyuchao1988@gmail.com
Department of Earth and Planetary Science, University of California, Berkeley, CA, USA
State Key Laboratory of Lithospheric Evolution, Institute of Geology and Geophysics, Chinese Academy of Sciences, Beijing, China
2. Liang Zhao
Email: zhaoliang@mail.iggcas.ac.cn
State Key Laboratory of Lithospheric Evolution, Institute of Geology and Geophysics, Chinese Academy of Sciences, Beijing, China
3. Yann Capdeville
Email: yann.capdeville@univ-nantes.fr
Laboratoire de Planétologie et Géodynamique de Nantes, CNRS, Université de Nantes
4. Zigen Wei
Email: weizigen@apm.ac.cn
State Key Laboratory of Geodesy and Earth's Dynamics, Innovation Academy for Precision Measurement Science and Technology, Chinese Academy of Sciences, Wuhan, China

8 List of Figure Captions

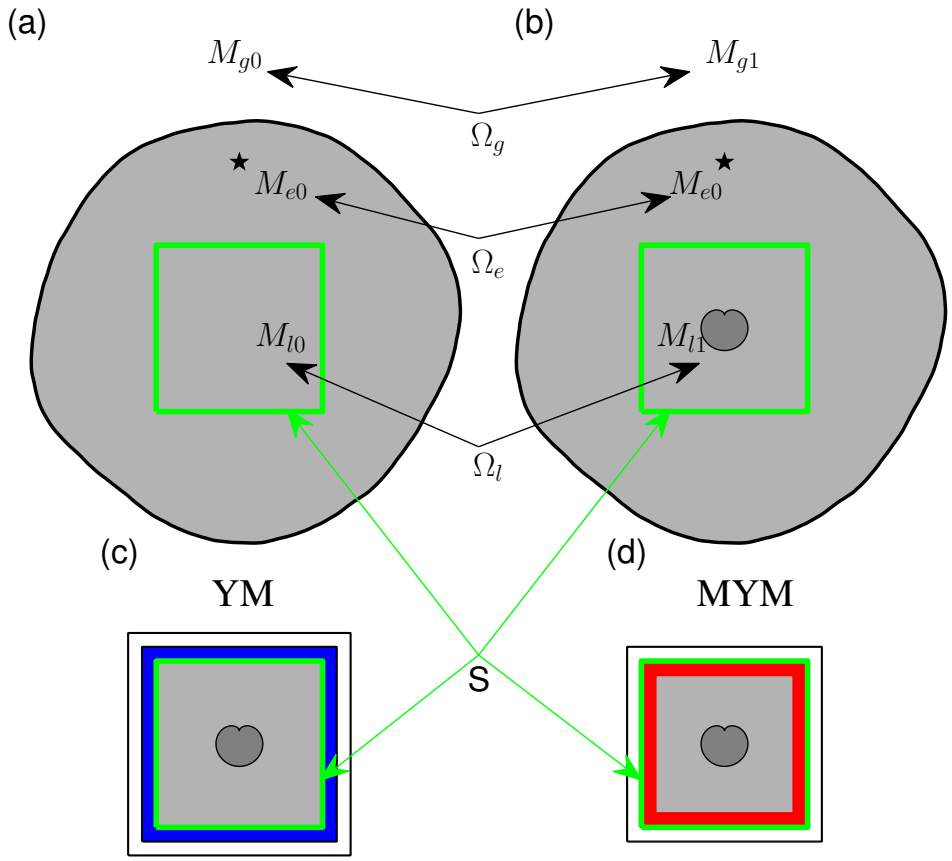

Figure 1. Nomenclatures of the global and hybrid simulations. (a) The global reference model M_{g0} contains the external model M_{e0} and the local reference model M_{l0} which are assigned to the global domain Ω_g, external domain Ω_e, and local domain Ω_l, respectively. The green line represents the hybrid interface S. (b) The global target model M_{g1} contains the same external model M_{e0} and the local target model M_{l1}, which are also assigned to the domains Ω_g, Ω_e, and Ω_l. The gray Cartesian circle represents the local target multi-scale heterogeneities. (c) The local target model M_{l1} and its hybrid interface S (green line) of the YM hybrid method, as well as the hybrid inputs, are imposed into the blue layer (hybrid elements for calculating the hybrid inputs). (d) The local target model M_{l1} and its hybrid interface S (green line) of the proposed MYM hybrid method, as well as the hybrid inputs, are imposed into the red layer (where the hybrid elements are located). The white layers in (c) and (d) represent the perfectly matched layer (PML) domains.

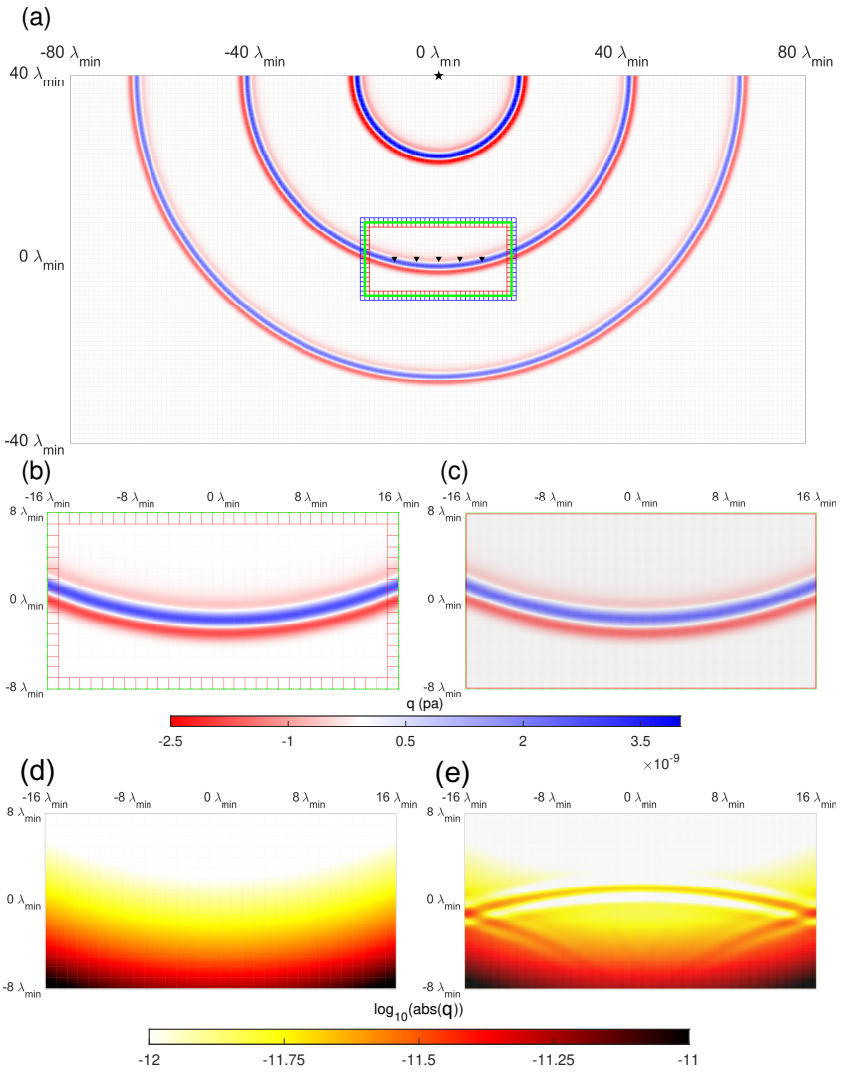

Figure 2. Wavefields of the global and hybrid simulations in the 2D reference homogeneous model. (a) 2D global homogeneous domain Ω_0 and wavefields. One source and five receivers are represented by the black star and inverse triangles, respectively. The mesh of 160 × 80 elements is displayed. The wavefields at the 24 $t_{\min}$, 48 $t_{\min}$, and 72 $t_{\min}$ time steps are superposed ($t_{\min} = 1/f_{\max}$). The green line comprising GLL points is the hybrid interface S of the local domain, and the blue and red elements are the hybrid elements used to implement the hybrid simulations in Masson et al. (2014) and this study, respectively. (b, c) 2D local homogeneous hybrid pressure (q) wavefields at 48 $t_{\min}$. (b) Hybrid wavefields calculated using the MYM method and the mesh of 32 × 16 elements associated with eight GLL points are displayed. (c) Local wavefields calculated using the MYM method based on spatial Lagrange interpolation and a different local mesh of 320 × 160 elements associated with three GLL points are displayed. The associated hybrid inputs are imposed on the green line around the red elements. (d, e) Pressure Wavefields at 63 $t_{\min}$ in hybrid simulations, (d) using the same local mesh as the global one, (e) using a different local mesh.

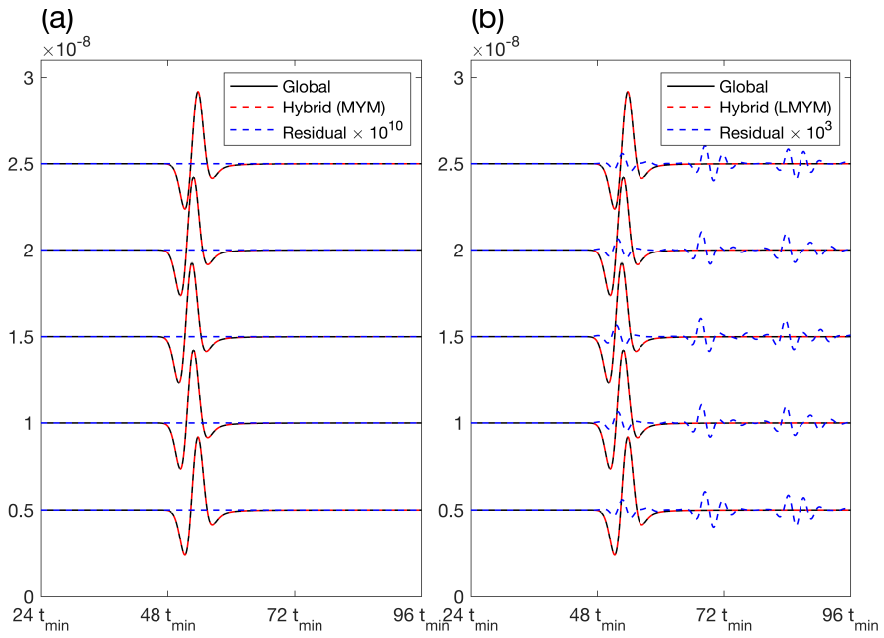

Figure 3. Waveform comparison between the global and hybrid simulations in the 2D homogeneous model. The solid black, the dashed red, and the dashed blue lines represent the global simulation, hybrid simulation, and their residual waveforms, respectively. (a) MYM method with the same local mesh as that in the global simulation. (b) MYM method with a different local mesh from that in the global simulation.

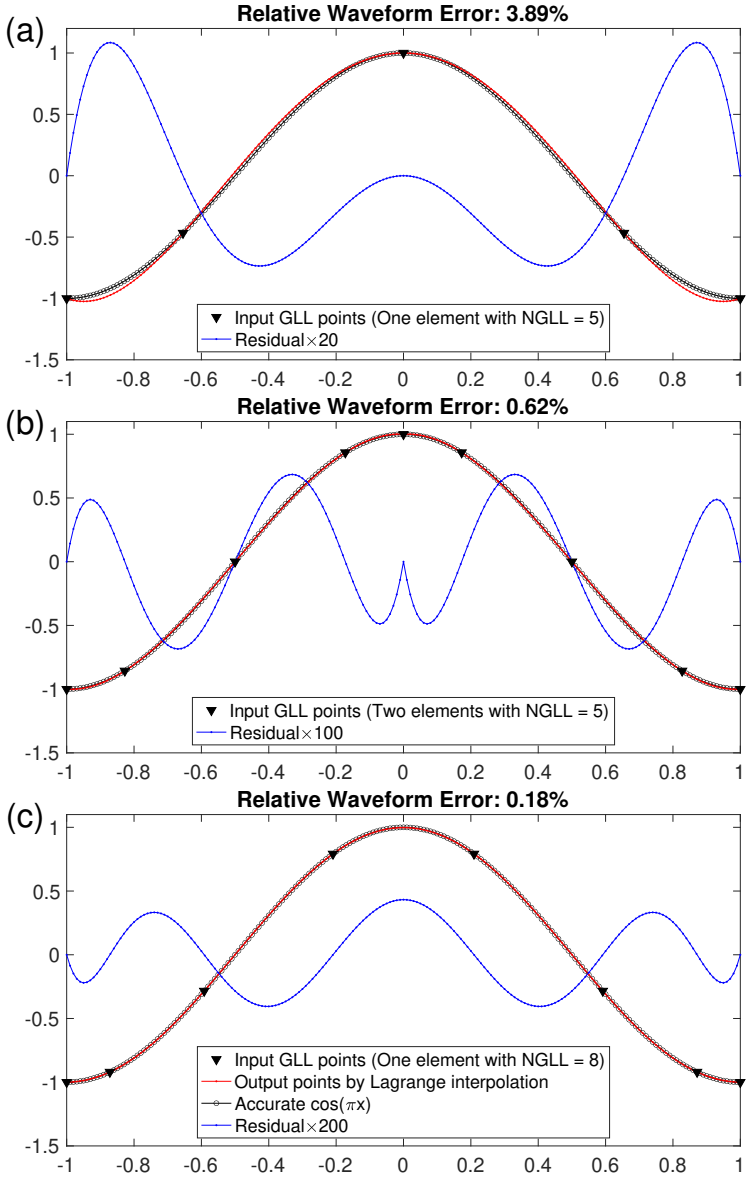

Figure 4. Error analysis of Lagrange interpolation in the spectral element method (SEM) framework for different spatial mesh. The reverse solid black triangles are the values of the $\cos(\pi x)$ function at the GLL points in the reference element $[-1,\ 1]$. The red points represent the output points between $[-1,\ 1]$ by Lagrange interpolation of the solid black triangles. The residual error between the red points and the accurate $\cos(\pi x)$ values (in black circles) are shown as blue points. (a) Only one element with $NGLL = 5$ in the reference element. (b) Two elements with $NGLL = 5$ in the reference element. (c) Only one element with $NGLL = 8$ in the reference element.

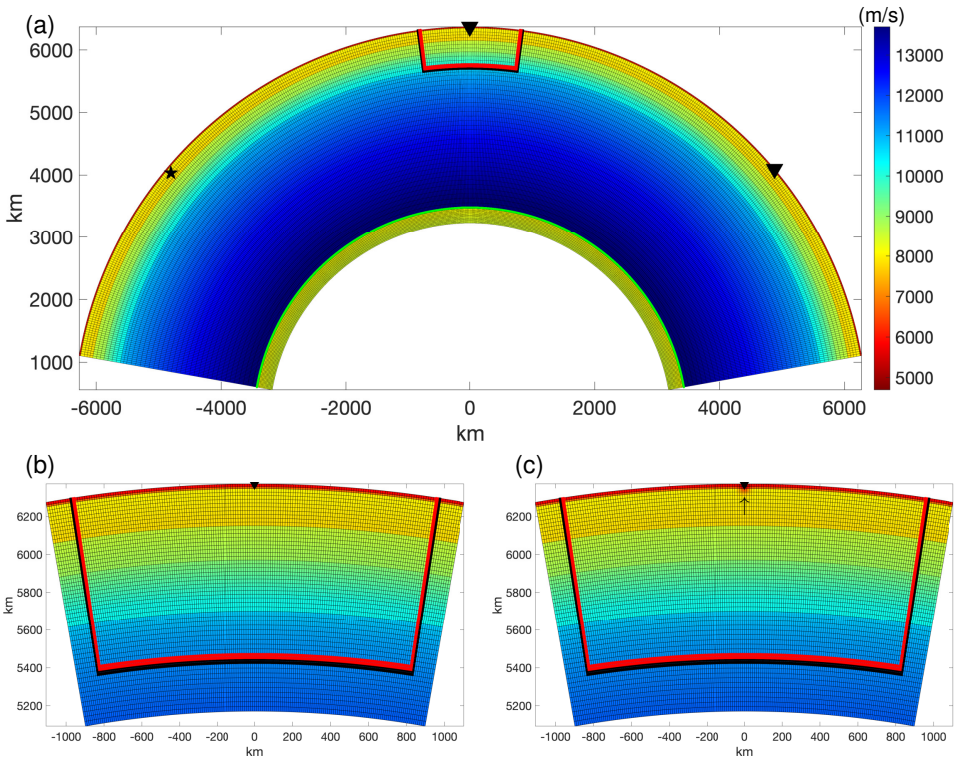

Figure 5. Models used in 2D global and hybrid numerical simulations. (a) Global reference model (P-wave velocity in PREM (Dziewonski & Anderson, 1981)) with the dimensions $(160^\circ, 2891km + 250km)$ including the entire Crust, Mantle, and 250km Outer Core below the CMB and $490 \times (44 + 12)$ structural elements. (b) Local reference model (P-wave velocity in PREM) with the dimensions $(20^\circ, 1200km)$ containing the entire Crust and part of the Mantle and 174×55 structural elements. (c) Local target model (P-wave velocity in PREM plus a Gaussian anomaly below the free surface). The size of the Gaussian anomaly is located $20km$ below the receiver with -20% V_p, -10% V_s, and -5% ρ reduction. The source and receiver are displayed in the black star and triangles. We use a remote Ricker wavelet source, with the main frequencies set from $f_0 = 1/15$ to $f_0 = 1/29$ Hz and the largest frequency $f_{\max} = 2.5 f_0$. The source S^e is located at $(-50^\circ, 6271$ km), 100km below the surface, where the angle is defined with the z-axis. Two receivers are placed: one R^i inside the box located at $(0^\circ, 6371$km), on the surface and another R^e outside the box located at $(50^\circ, 6371$ km). All the GLL points used to impose the hybrid inputs are in black, and the GLL points used to calculate the hybrid outputs for the receiver outside the box are in red. The black and red GLL points in (a), (b), and (c) are the same, which are all originally from the local domain. The global mesh is prepared to accurately simulate a minimum period of 6 seconds.

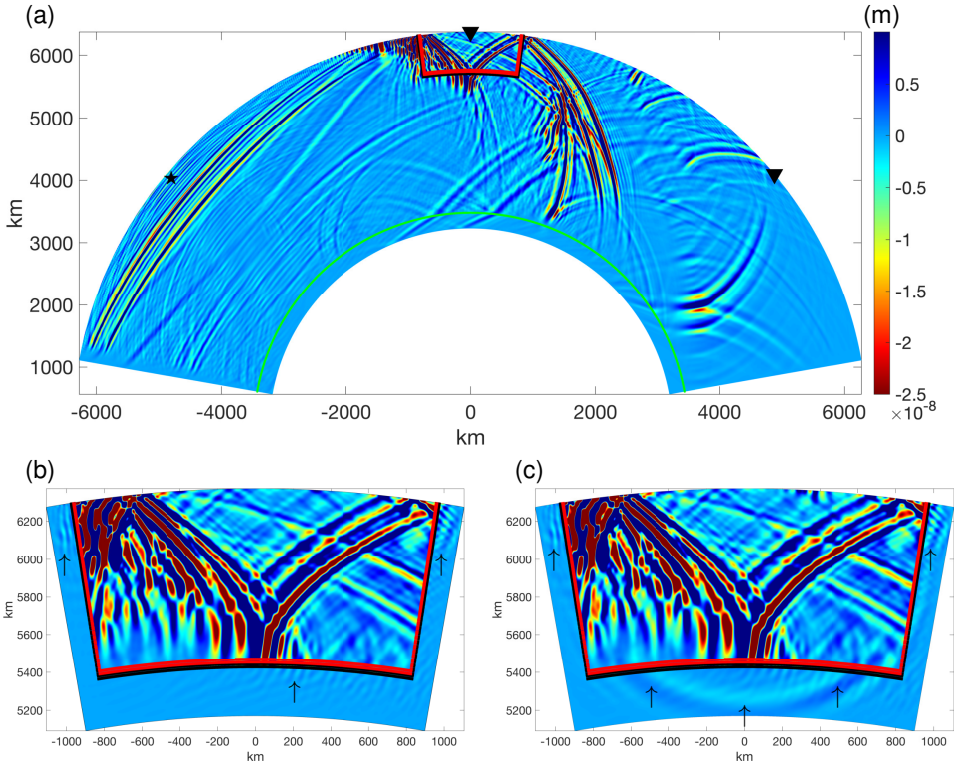

Figure 6. The wavefields at approximately 1100 seconds are depicted in (a) the global reference PREM model, (b) the local reference model, and (c) the local target (Gaussian) model.

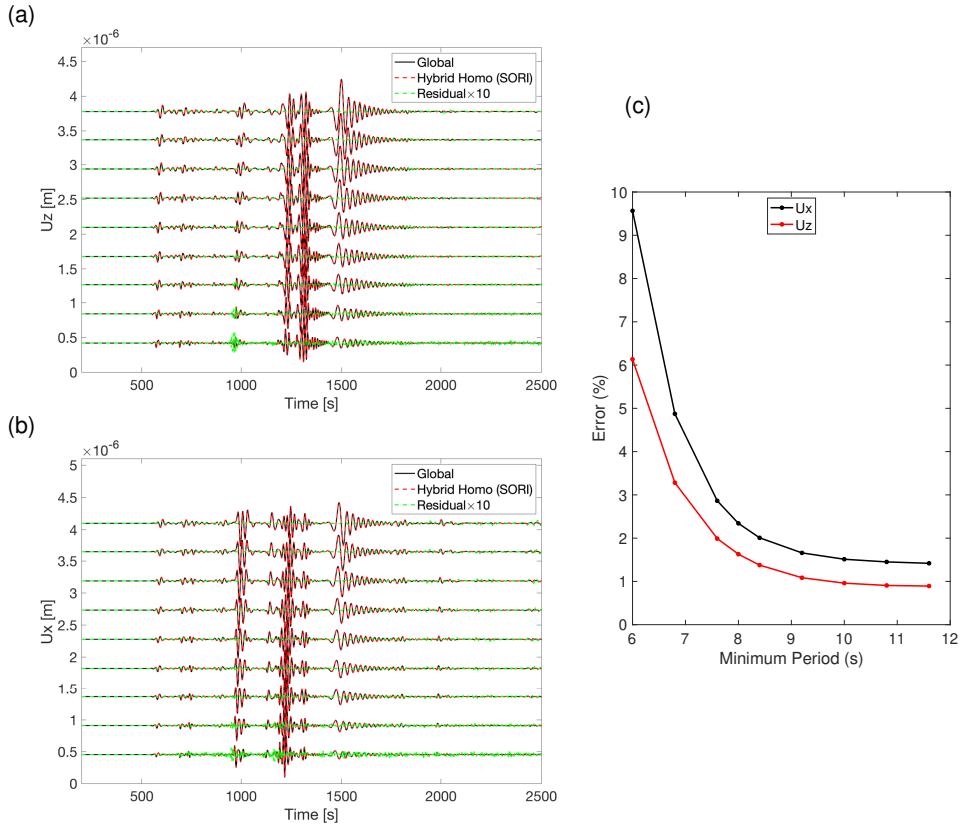

Figure 7. Waveforms and errors of the Receiver inside the local model in various frequency bands under the 1D PREM (Dziewonski & Anderson, 1981) with 2D numerical simulation: (a, b) The x and z displacements in solid black are calculated using the global reference PREM model, while the x and z in dashed red displacements are computed using the local reference PREM model within the hybrid simulation. The residual waveforms in solid green are magnified by a factor of 10. (c) The L1 norm of the errors in the x and z components exhibits an inverse relationship with the minimum periods of the Ricker wavelet used. Note that the global and local meshes differ from each other, they remain consistent for each minimum period. The global mesh is designed for a minimum period of 6 seconds, and the local mesh is denser than the global one for generating small-scale structures.

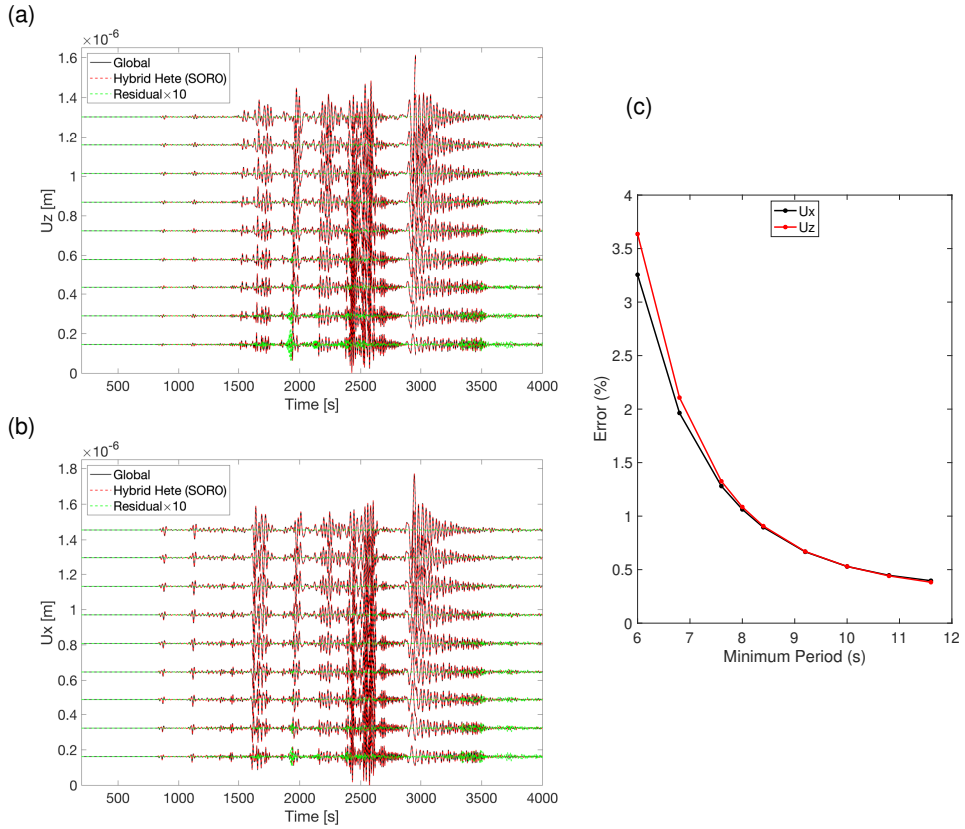

Figure 8. Waveforms and errors of the receiver outside the local model in various frequency bands within a global target model (PREM plus Gaussian anomaly), using 2D numerical simulation. (a, b) The x and z displacements in solid black are calculated within the global target model, while the x and z displacements in dashed red are obtained by summing the hybrid waveform (via convolution (Adourian et al., 2022)), and global reference waveform. The residual waveforms in solid green are magnified by a factor of 10. (c) The L1 norm of the errors in the x and z components exhibits an inverse relationship with the minimum periods of the Ricker wavelet used. The global and local meshes are the same as Figure 7. The proposed method for enhancing the accuracy of hybrid simulation also applies to receivers located outside the box.

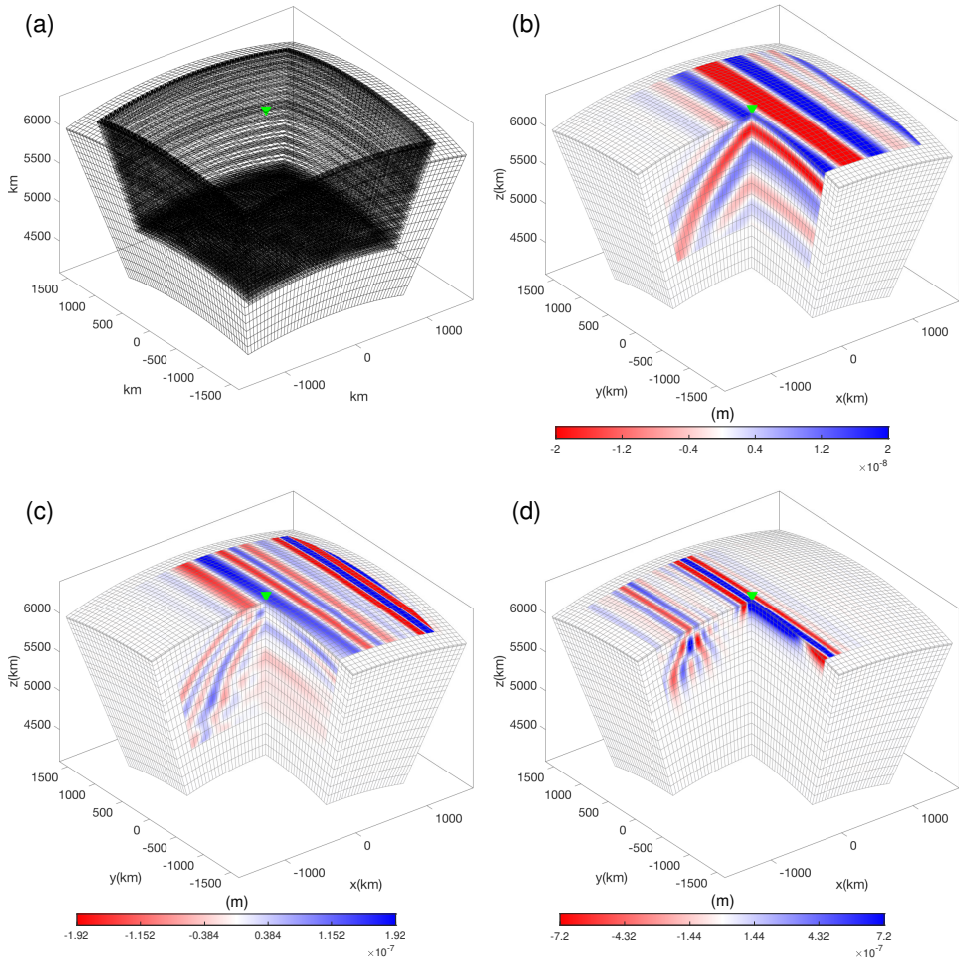

Figure 9. Local mesh, hybrid GLL points, and wavefields of Z component that are generated in 3D hybrid numerical simulations. (a) The local domain covers dimensions of $(30^\circ, 30^\circ, 2000km)$, including the entire crust and part of the mantle. The local simulations use the structured mesh consisting of $49 \times 49 \times 20$ elements, designed to simulate a minimum period of 27 seconds. The receiver is depicted as a green reversed triangle, R^i, at $(90^\circ, 0^\circ, 6371km)$, while the 328125 GLL points used to impose the hybrid inputs are shown in black. Three hybrid wavefields, corresponding to arrival times of P, S, and Surface wave phases at around 520, 980, and 1460 seconds, are plotted in (b), (c), and (d), respectively. Four elements are used as the absorbing layer. The hybrid inputs are calculated by the program SPECFEM3D_GLOBE from a teleseismic event.

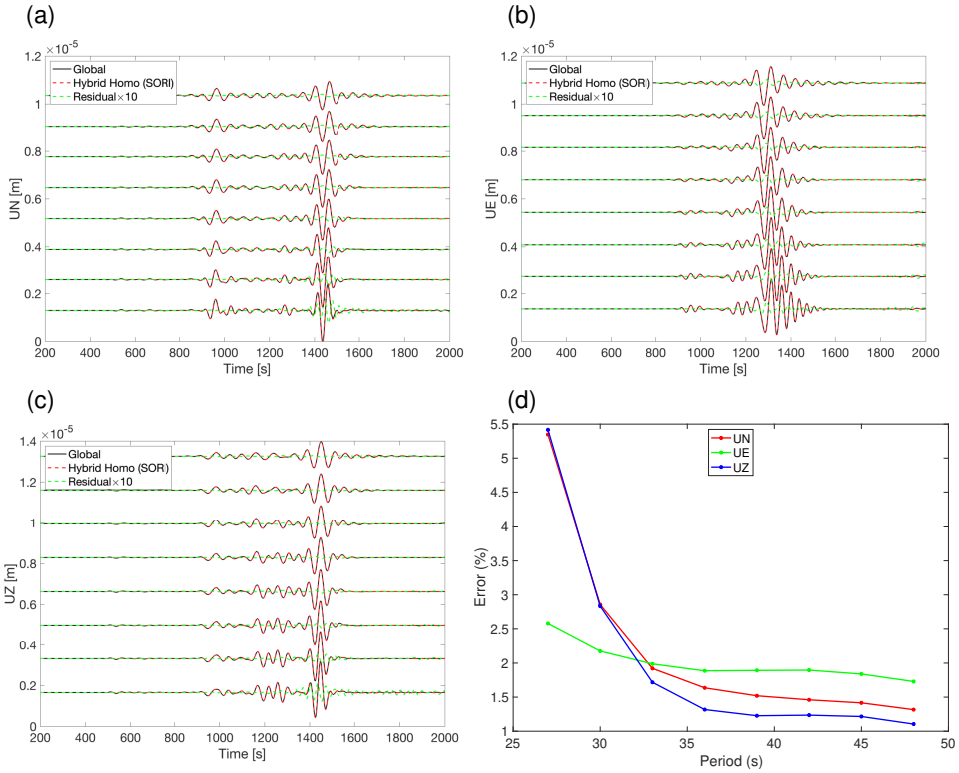

Figure 10. Waveforms and errors of the receiver inside the local model in various frequency bands under the 1D PREM (Dziewonski & Anderson, 1981) with the 3D hybrid numerical simulations. (a,b,c) The displacements of N, E, and Z components in solid black are calculated using the global reference PREM model, while the dashed red displacements are computed using the local reference PREM model during the hybrid simulation. The residual waveforms in solid green are magnified by a factor of 10. (d) The L1 norm of the errors in the N, E, and Z components exhibit an inverse relationship with the first cutoff corner period of the Heaviside wavelet used, from 27, 30, to 48 s. Note that the global and local meshes differ from each other, but they remain consistent for each different cutoff corner period, both being designed for a main period of 27 seconds.